Science Advances
AAAS

advances.sciencemag.org/cgi/content/full/6/35/eabb4641/DC1

Supplementary Materials for

3D printed patient-specific aortic root models with internal sensors for minimally invasive applications

Ghazaleh Haghiashtiani, Kaiyan Qiu, Jorge D. Zhingre Sanchez, Zachary J. Fuenning, Priya Nair, Sarah E. Ahlberg, Paul A. Iaizzo, Michael C. McAlpine*

*Corresponding author. Email: mcalpine@umn.edu

Published 28 August 2020, *Sci. Adv.* **6**, eabb4641 (2020)
DOI: 10.1126/sciadv.abb4641

The PDF file includes:

Other Supplementary Material for this manuscript includes the following:

(available at advances.sciencemag.org/cgi/content/full/6/35/eabb4641/DC1)

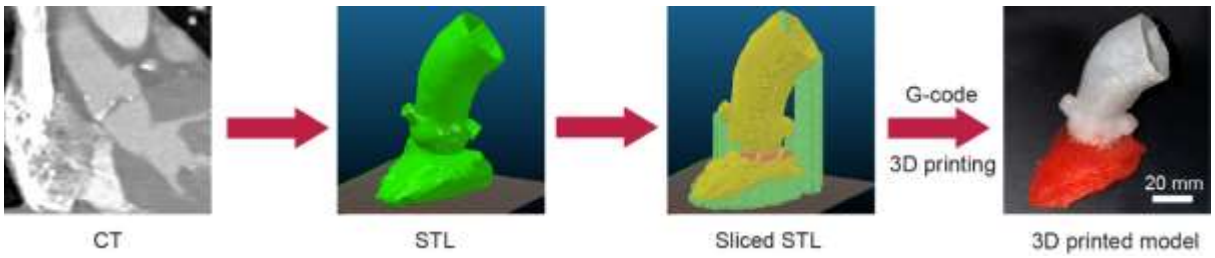

Fig. S1. Process for generating the G-code for 3D printing of the patient-specific aortic root model. [Photo credit: Ghazaleh Haghiashtiani and Kaiyan Qiu, University of Minnesota]

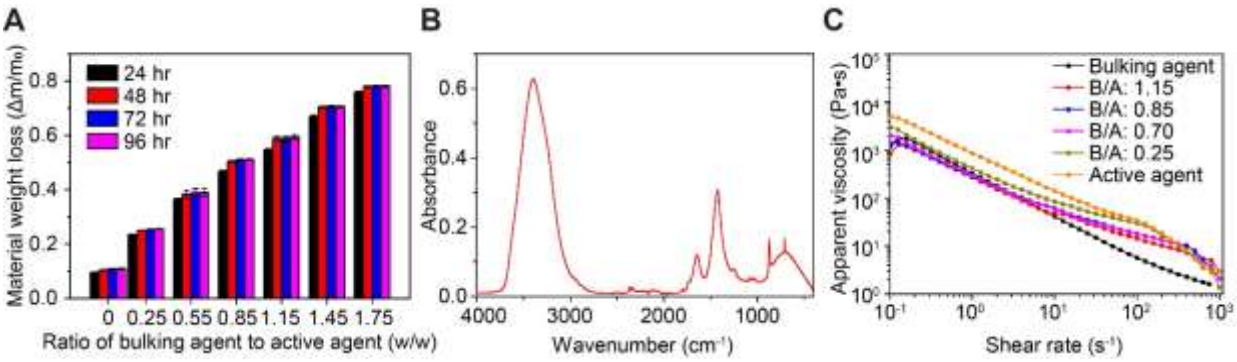

Fig. S2. Additional material characterization results. (A) Ratio of material weight loss for different compositions of the customized polymeric material in hexane at different time stamps of immersion in the solvent (N = 3). **(B)** FTIR plot of the calcification material. **(C)** Viscometry data of different custom-formulated polymeric inks and comparison to bulking and active agents.

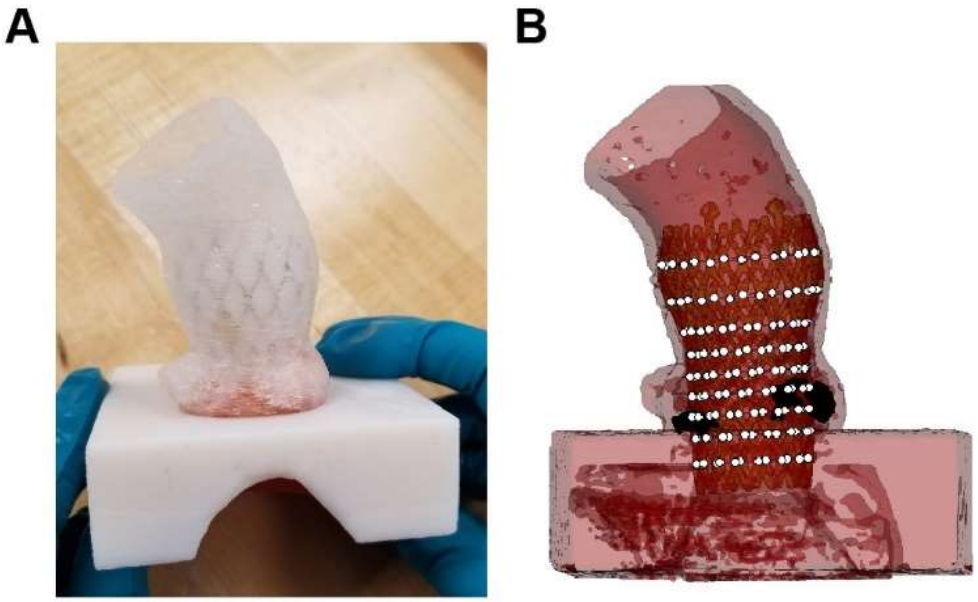

Fig S3. Implantation of the bioprosthetic valve in the 3D printed aortic root model. (**A**) Implanted valve in the 3D printed aortic root model mounted in the fixture. [Photo credit: Priya Nair and Sarah Ahlberg, Medtronic] (**B**) Corresponding scan of the 3D printed model constructed from CT imaging and the marked 9 node levels used for frame analysis.

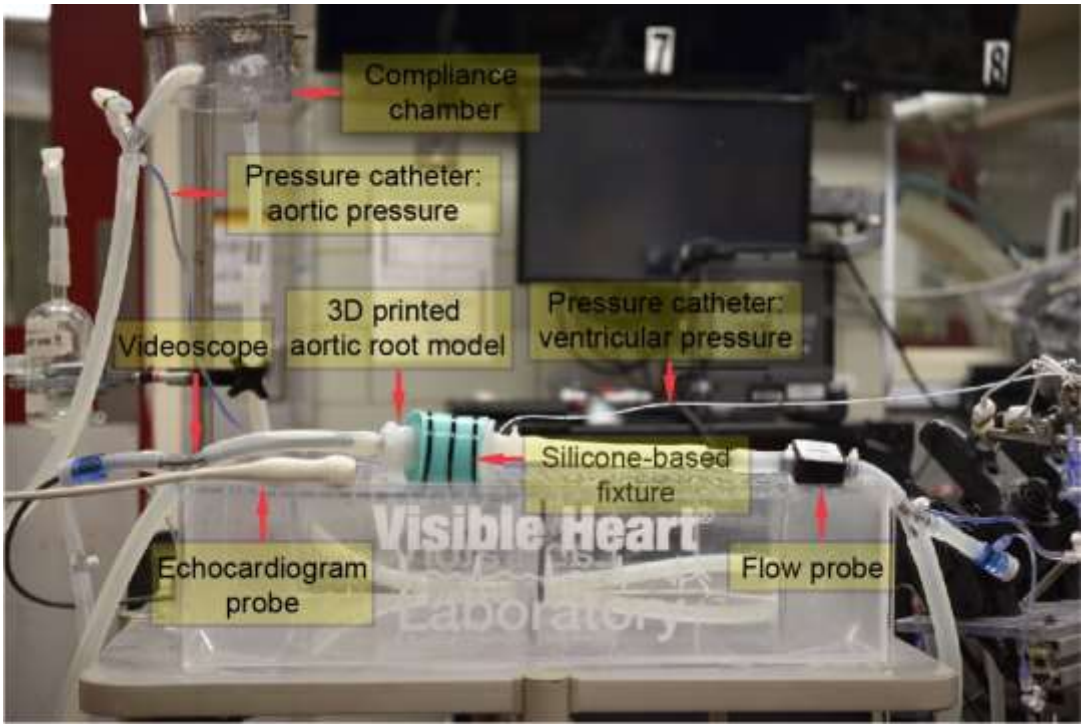

Fig. S4. Test setup for *in vitro* hemodynamic studies. [Photo credit: Ghazaleh Haghiashtiani and Kaiyan Qiu, University of Minnesota]

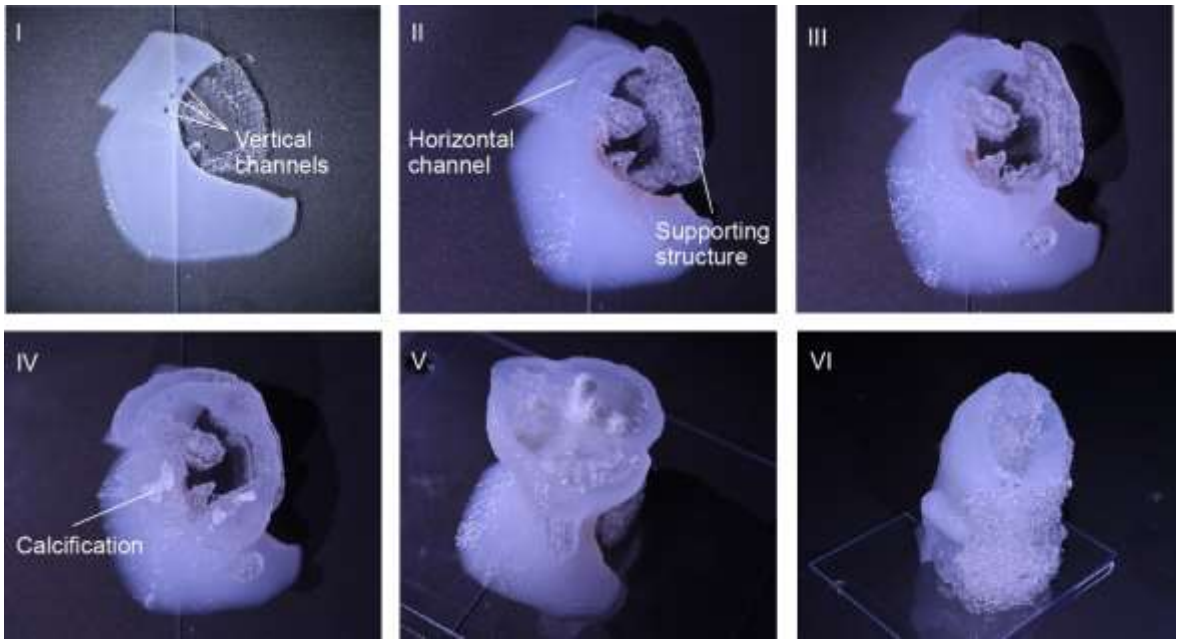

Fig S5. Step-by-step 3D printing of the aortic root model with internally integrated sensor array. [Photo credit: Ghazaleh Haghiashtiani and Kaiyan Qiu, University of Minnesota]

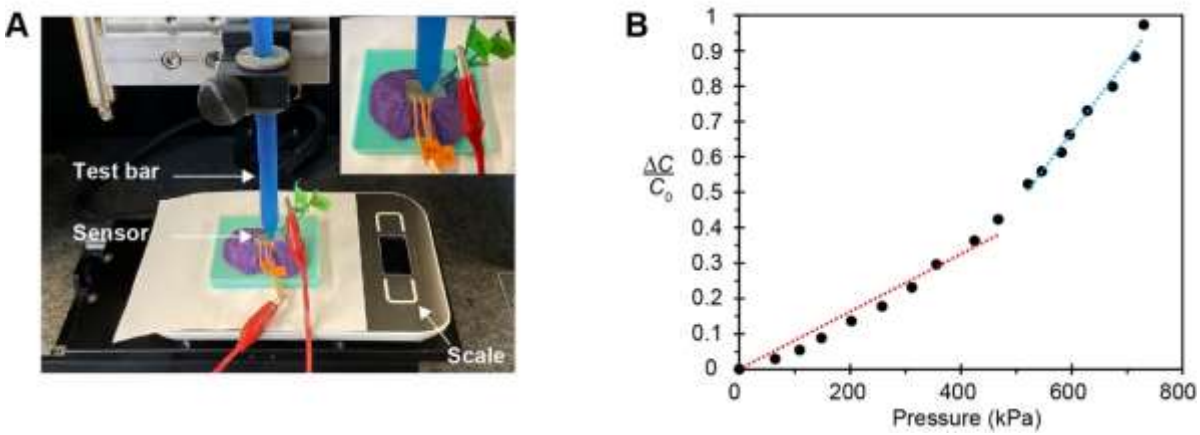

Fig. S6. Calibration of the sensor array. (**A**) Test setup (inset: close-up view of the test bar pressing on a sensing element). [Photo credit: Ghazaleh Haghiashtiani and Kaiyan Qiu, University of Minnesota] (**B**) An example of calibration plot for the sensing elements indicating the two corresponding linear regions.

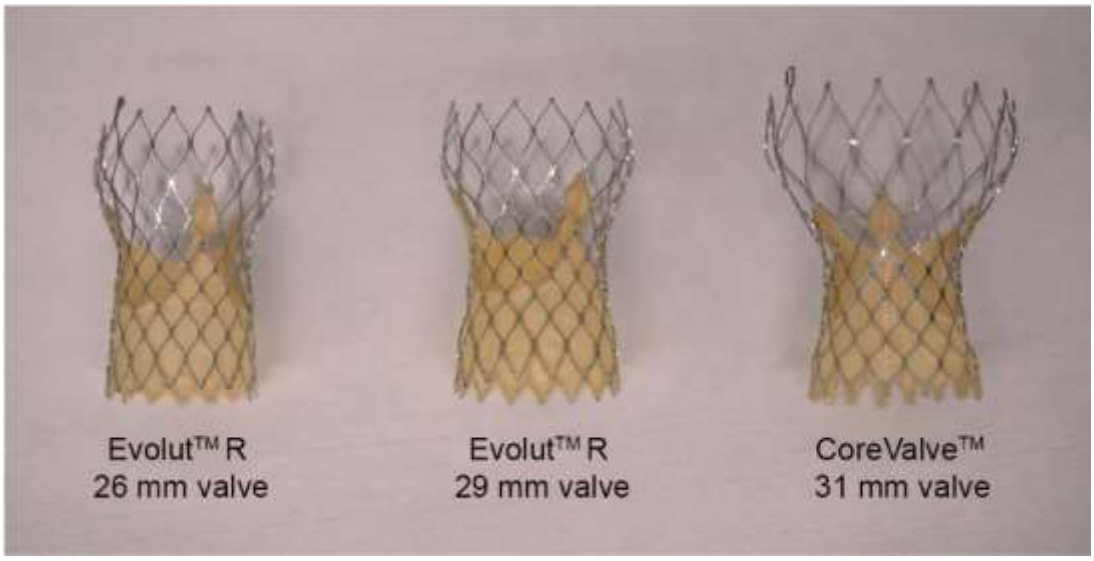

Fig. S7. Medtronic bioprosthetic TAVR valves used in different case studies. [Photo credit: Ghazaleh Haghiashtiani and Kaiyan Qiu, University of Minnesota]

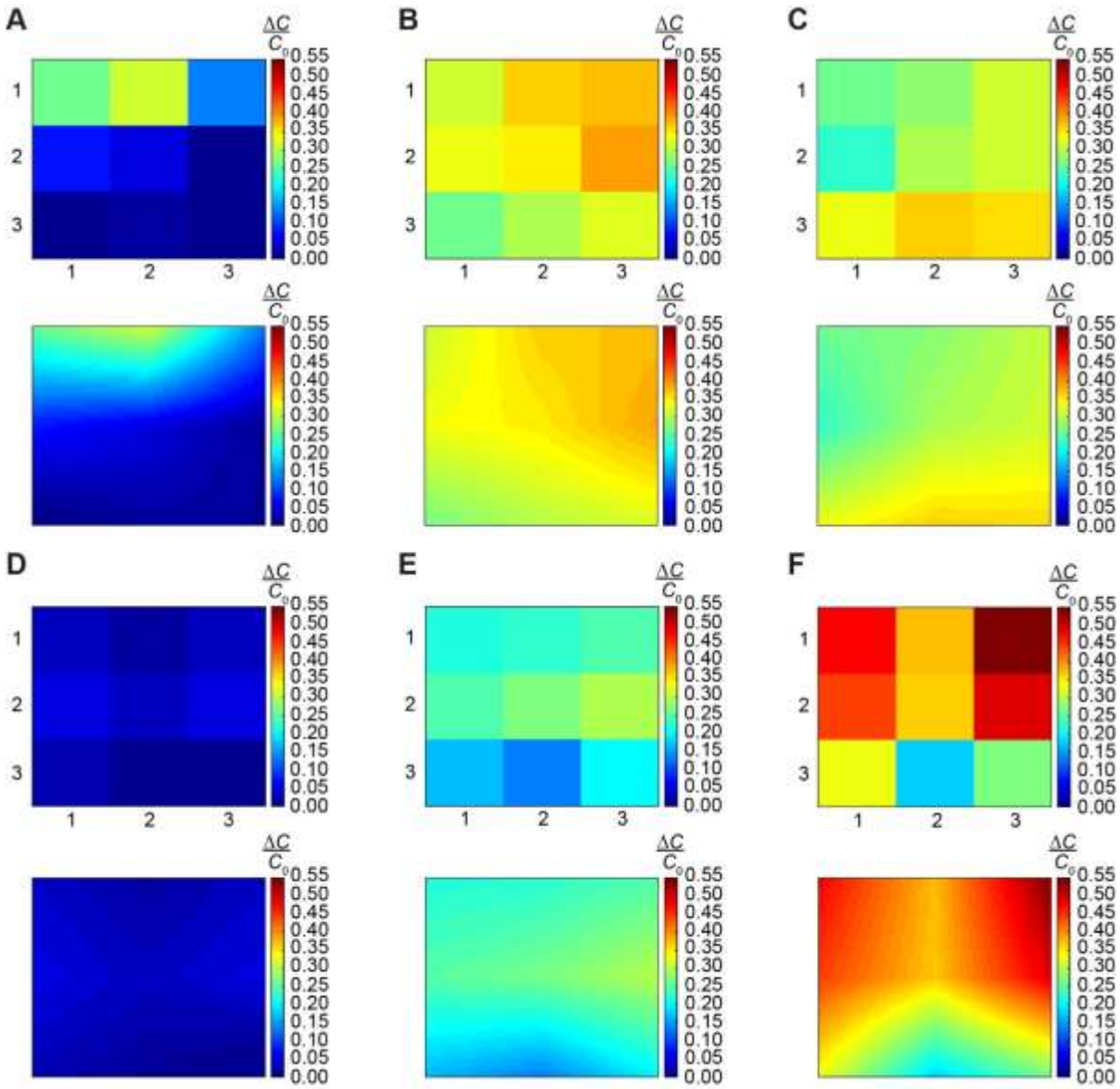

Fig. S8. Heatmaps of normalized capacitance changes for different cases of valve implantation height and sizing. (**A**) Implantation of the 29 mm Evolut™ R TAVR valve frame at a shallow height. (**B**) Implantation of the 29 mm Evolut™ R TAVR valve frame at an intermediate height. (**C**) Implantation of the 29 mm Evolut™ R TAVR valve frame at a deep height. (**D**) Implantation of the 26 mm Evolut™ R TAVR valve at an intermediate height. (**E**) Implantation of the 29 mm Evolut™ R TAVR valve at an intermediate height. (**F**) Implantation of the 31 mm CoreValve™ TAVR valve at an intermediate height. Top plots in each panel represent the 3 × 3 discrete heatmap for each case; bottom plots in each panel represent the continuous heatmaps resulted from interpolation and halving the intervals 5 times in each dimension.

Table S1. Estimated elastic modulus of examples of tissue and custom-formulated polymer samples at different strains and comparison with reported values in the literature. (ε: strain; B/A: weight ratio of bulking agent to active agent in the composition, N=3)

Sample Type	Young's Modulus at $\boldsymbol{\varepsilon < 0.03}$ (kPa)	Tangent Modulus at $\boldsymbol{\varepsilon \sim 0.10}$ (kPa)	Tangent Modulus at $\boldsymbol{\varepsilon \sim 0.30}$ (kPa)	Reported Modulus Values in Literature (kPa)
Human myocardium tissue	36-146	54-267	168-732	12-273 *(30, 31)*
Human aortic tissue	56-216	112-1,077	533-1,097	334-1,817 *(32, 33)*
Ink 1 (B/A=1.15)	113.4 ± 3.7	99.1 ± 3.8	162.7 ± 17.5	
Ink 2 (B/A=0.85)	165.8 ± 8.5	194.7 ± 20.8	213.3 ± 19.0	
Ink 3 (B/A=0.7)	250.6 ± 9.1	260.1 ± 25.4	284.0 ± 5.1	
Ink 4 (B/A=0.25)	455.6 ± 22.5	712.7 ± 13.9	679.2 ± 24.8	

Table S2. Calibration equations for the 9 sensing elements of the sensor array.

Sensing Element (row, column)	$\frac{\Delta C}{C_0}$ Range	Calibration Equation
Element 11	$\frac{\Delta C}{C_0} \leq 0.35$	$P = \left(\frac{\Delta C}{C_0}\right) / 0.0011$
	$\frac{\Delta C}{C_0} > 0.35$	$P = \left(\frac{\Delta C}{C_0} + 0.5222\right) / 0.0032$
Element 12	$\frac{\Delta C}{C_0} \leq 0.14$	$P = \left(\frac{\Delta C}{C_0}\right) / 0.0009$
	$\frac{\Delta C}{C_0} > 0.14$	$P = \left(\frac{\Delta C}{C_0} + 0.3407\right) / 0.0029$
Element 13	$\frac{\Delta C}{C_0} \leq 0.45$	$P = \left(\frac{\Delta C}{C_0}\right) / 0.0008$
	$\frac{\Delta C}{C_0} > 0.45$	$P = \left(\frac{\Delta C}{C_0} + 0.5656\right) / 0.0021$
Element 21	$\frac{\Delta C}{C_0} \leq 0.17$	$P = \left(\frac{\Delta C}{C_0}\right) / 0.0011$
	$\frac{\Delta C}{C_0} > 0.17$	$P = \left(\frac{\Delta C}{C_0} + 0.9813\right) / 0.006$
Element 22	$\frac{\Delta C}{C_0} \leq 0.2$	$P = \left(\frac{\Delta C}{C_0}\right) / 0.0009$
	$\frac{\Delta C}{C_0} > 0.2$	$P = \left(\frac{\Delta C}{C_0} + 0.4778\right) / 0.0032$
Element 23	$\frac{\Delta C}{C_0} \leq 0.4$	$P = \left(\frac{\Delta C}{C_0}\right) / 0.0008$
	$\frac{\Delta C}{C_0} > 0.4$	$P = \left(\frac{\Delta C}{C_0} + 0.1276\right) / 0.0013$
Element 31	$\frac{\Delta C}{C_0} \leq 0.07$	$P = \left(\frac{\Delta C}{C_0}\right) / 0.0004$
	$\frac{\Delta C}{C_0} > 0.07$	$P = \left(\frac{\Delta C}{C_0} + 0.3474\right) / 0.002$
Element 32	$\frac{\Delta C}{C_0} \leq 0.45$	$P = \left(\frac{\Delta C}{C_0}\right) / 0.0009$
	$\frac{\Delta C}{C_0} > 0.45$	$P = \left(\frac{\Delta C}{C_0} + 0.5949\right) / 0.0024$
Element 33	$\frac{\Delta C}{C_0} \leq 0.11$	$P = \left(\frac{\Delta C}{C_0}\right) / 0.0007$
	$\frac{\Delta C}{C_0} > 0.11$	$P = \left(\frac{\Delta C}{C_0} + 0.4501\right) / 0.0031$